CSIRO PUBLISHING
www.publish.csiro.au/journals/eg
Exploration Geophysics, 2007, **38**, 69–76

Numerical modelling of electromagnetic waveguide effects on crosshole radar measurements

Hannuree Jang[1,2] Mi Kyung Park[1] Hee Joon Kim[1]

[1]Department of Environmental Exploration Engineering, Pukyong National University, Busan 608-737, Korea.
[2]Corresponding author. Email: jhnree@pknu.ac.kr

Abstract. High-frequency electromagnetic (EM) wave propagation associated with borehole ground-penetrating radar (GPR) is a complicated phenomenon. To improve the understanding of the governing physical processes, we employ a finite-difference time-domain solution of Maxwell's equations in cylindrical coordinates. This approach allows us to model the full EM wavefield associated with crosshole GPR surveys. Furthermore, the use of cylindrical coordinates is computationally efficient, correctly emulates the three-dimensional geometrical spreading characteristics of the wavefield, and is an effective way to discretise explicitly small-diameter boreholes. Numerical experiments show that the existence of a water-filled borehole can give rise to a strong waveguide effect which affects the transmitted waveform, and that excitation of this waveguide effect depends on the diameter of the borehole and the length of the antenna.

Key words: crosshole, cylindrical coordinates, GPR, finite-difference time-domain.

Introduction

Over the past decade, borehole ground-penetrating radar (GPR) has become increasingly popular as a tool for high-resolution imaging of the shallow subsurface. Applications of this technique include delineation of ore bodies (Fullagar et al., 2000), location of underground tunnels and voids (Olhoeft, 1988; Moran and Greenfield, 1993), mapping fractures in bedrock (Olsson et al., 1992; Day-Lewis et al., 2003), and estimation of subsurface lithology and hydrogeological properties using field- or laboratory-derived petrophysical relationships (Alumbaugh and Chang, 2002; Moysey and Knight, 2004; Tronicke et al., 2004).

Crosshole GPR tomography is identical in principle to seismic tomography. A transmitter antenna, moved to numerous locations in one borehole, radiates high-frequency electromagnetic (EM) pulses that are recorded by a receiver antenna, which is moved down a second borehole. Most commonly, inversion of the resulting data is accomplished by assuming that the propagating radar energy can be modelled by infinite-frequency rays that join the centres of the antennas. Under this assumption, first-break traveltimes and amplitudes of the data can be used to determine the distribution of subsurface EM-wave velocity and attenuation. The resulting ray-based tomographic images of the subsurface, however, are limited in resolution to approximately the width of the first Fresnel zone associated with the propagating pulse bandwidth (Williamson and Worthington, 1993). In order to improve resolution, we require modelling algorithms that account for more detailed physical aspects of the crosshole GPR experiment, such as wave propagation and antenna behaviour. These algorithms can be employed in waveform-based inversion strategies that use all of the recorded data to determine subsurface properties (e.g. Pratt and Worthington, 1988; Zhou et al., 1995).

There are several approaches to crosshole GPR modelling. None of these, however, allow for the simulation of both antenna transmission and reception in heterogeneous media. Sato and Thierbach (1991), for example, analytically modelled a crosshole GPR experiment using an expression for the current on an insulated dipole antenna derived by King and Smith (1981). Although their approach gives much insight into the effects of antenna and system parameters on recorded GPR wavelets, it requires a homogeneous medium between the boreholes and that the antennas are each in the far field of the other. In addition, the expression used for the antenna current is invalid for the case of water-filled boreholes and is thus only suitable for modelling in the vadose zone. Holliger and Bergmann (2002), on the other hand, numerically modelled crosshole GPR using a finite-difference time-domain (FDTD) approach in two-dimensional (2D) cylindrical coordinates. In their formulation, only the transmitter borehole was included in the model, and the antennas were simulated as point vertical electric dipoles. Ernst et al. (2006) further developed this algorithm to allow for detailed modelling of a realistic, finite-length transmitter antenna. Ellefsen and Wright (2005) employed a similar approach to examine the radiation patterns of realistic borehole GPR antennas. With these methods, much can be learned about the effects of the borehole, subsurface heterogeneity, and antenna characteristics on crosshole GPR radiation.

We present an algorithm to efficiently simulate crosshole GPR transmission in heterogeneous media. This is accomplished using FDTD modelling in 2D cylindrical coordinates. The algorithm can be easily implemented using a perfectly matched layer (PML) for absorbing boundaries, frequency-dependent media, and a finite-length transmitter antenna. The approach allows us to systematically explore the effects of various complicating factors on the radiated GPR signals. In this paper, we examine waveguide effects due to the existence of a water-filled borehole, and show that guided waves are affected by the diameter of the borehole, the length of the antenna, and the shape of transmitting signal.

10.1071/EG07008 0812-3985/07/010069

FDTD in 2D cylindrical coordinates

We start with the following Maxwell's equations

$$\frac{\partial \mathbf{D}}{\partial t} = \nabla \times \mathbf{H} \tag{1}$$

$$\mathbf{D}(\omega) = \varepsilon_0 \cdot \varepsilon_r^*(\omega) \cdot \mathbf{E}(\omega) \tag{2}$$

$$\frac{\partial \mathbf{H}}{\partial t} = -\frac{1}{\mu_0} \nabla \times \mathbf{E} \tag{3}$$

where $\mathbf{D}$ ($\mathrm{C\,m^{-2}}$) is the electric flux density, $\mathbf{E}$ ($\mathrm{V\,m^{-1}}$) is the electric field, $\mathbf{H}$ ($\mathrm{A\,m^{-1}}$) is the magnetic field, ω (Hz) is the angular frequency, ε_0 ($=8.854 \times 10^{-12}\,\mathrm{F\,m^{-1}}$) and μ_0 ($=4\pi \times 10^{-7}\,\mathrm{H\,m^{-1}}$) are dielectric permittivity and magnetic permeability in free space, respectively, and

$$\varepsilon_r^*(\omega) = \varepsilon_r + \frac{\sigma}{j\omega\varepsilon_0} \tag{4}$$

where ε_r is the relative dielectric constant, and σ ($\mathrm{S\,m^{-1}}$) is the conductivity. In this formulation, it is assumed that the materials being simulated are nonmagnetic; that is $\mathbf{H} = \mathbf{B}/\mu_0$, where $\mathbf{B}$ ($\mathrm{Wb\,m^{-2}}$) is the magnetic induction. There is a reason for using this formulation; equations (1) and (3) remain the same regardless of the material, and any complicated mathematics stemming from the material is in equation (2). The solution of equation (2) can be viewed as a digital filtering problem (Sullivan, 2000), and the simulation of frequency-dependent media, for example, can be easily addressed.

We further normalise Maxwell's equations by substituting

$$\tilde{\mathbf{E}} = \sqrt{\frac{\varepsilon_0}{\mu_0}}\mathbf{E} \approx \frac{\mathbf{E}}{120\pi} \tag{5}$$

$$\tilde{\mathbf{D}} = \frac{\mathbf{D}}{\sqrt{\varepsilon_0 \mu_0}} = c_0 \mathbf{D} \tag{6}$$

where c_0 ($\mathrm{m\,s^{-1}}$) is the speed of light. This is the system of Gaussian (CGS) units. The reason for using it is simplicity in the formulation. The electric and magnetic fields have the same order of magnitude. This has an advantage in formulating PML, which is a crucial part of FDTD simulation.

The core of our modelling approach is the FDTD solution of Maxwell's equations in 2D cylindrical coordinates. In this formulation, rotational symmetry about the vertical z-axis is assumed so that Maxwell's equations can be separated into the transverse electric (TE) and transverse magnetic (TM) modes, which are two sets of coupled partial-differential equations involving the (E_ϕ, H_ρ, H_z) and (E_ρ, E_z, H_ϕ) components, respectively. For crosshole GPR modelling where the antennas are oriented parallel to the z-axis, only the TM-mode equations are required. Dropping the ~ notation, Maxwell's equations are reduced in TM mode to

$$\frac{\partial D_\rho}{\partial t} = -c_0 \frac{\partial H_\phi}{\partial z} \tag{7}$$

$$\frac{\partial D_z}{\partial t} = c_0 \left[\frac{1}{\rho}\frac{\partial (\rho H_\phi)}{\partial \rho}\right] \tag{8}$$

$$D(\omega) = \varepsilon_r^* \cdot E(\omega) \tag{9}$$

$$\frac{\partial H_\phi}{\partial t} = c_0 \left(\frac{\partial E_z}{\partial \rho} - \frac{\partial E_\rho}{\partial z}\right). \tag{10}$$

These equations are solved numerically in the time domain using a leapfrog, staggered-grid approach, which involves offsetting the electric- and magnetic-field components so that the FD approximations of all partial derivatives are centred in both space and time (Yee, 1966). Stepping forward in time is accomplished by alternately updating the electric and magnetic fields. All updates are explicit.

We locate our field components in space identically to Holliger and Bergmann (2002) to avoid singularity problems associated with equation (8) on the z-axis, as shown in Figure 1; there is no E_z component located at $\rho = 0$. Figure 1 also shows the allocation of electric- and magnetic-field components on each cell; the electric- and magnetic-field components are located at the edges and the centre of a cell, respectively. Because the electric fields are set to cell edges, an averaged conductivity and permittivity must be evaluated at the edges (see Appendix).

We choose the time step Δt according to the Courant numerical stability criterion

$$\Delta t \leq \frac{1}{c_{\max}\sqrt{(1/\Delta\rho)^2 + (1/\Delta z)^2}} \tag{11}$$

where $\Delta\rho$ and Δz are the discretisation sizes along the ρ and z axes, respectively, and $c_{\max} = 1/(\varepsilon_{\min}\mu_0)^{1/2}$ is the maximum phase velocity in the FD grid, with $\varepsilon_{\min}$ being the lowest value of the dielectric permittivity.

We also use second-order-accurate FD approximations for all derivatives, which mean that ten grid-points per minimum wavelength are needed to control numerical dispersion. Higher-order approximations can be used for the spatial and temporal derivatives in our code, with a moderate increase in code complexity, in order to decrease the number of field points required, and thus reduce computing time (e.g. Bergmann et al., 1999).

Waveguide effects

For numerical simulations we use a FD grid consisting of 510×1200 cells and uniform cell width of $\Delta\rho = \Delta z = 1$ cm. We implement PML absorbing boundaries in cylindrical coordinates to prevent reflections from the top, bottom,

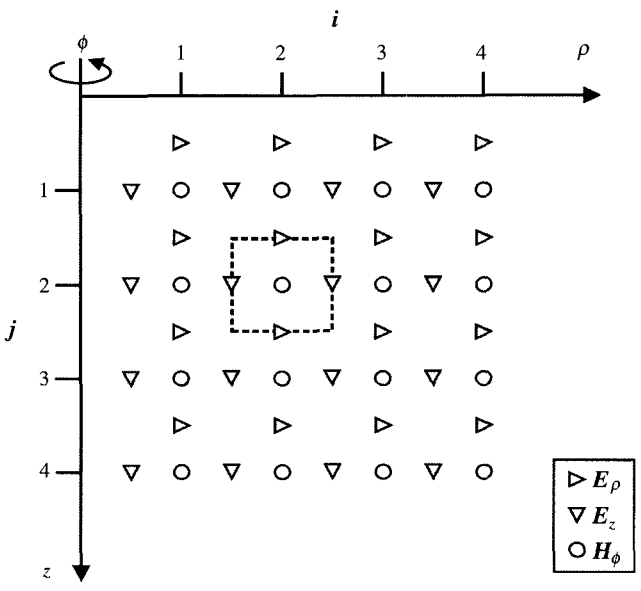

Fig. 1. The staggered FD grid used to discretise Maxwell's equations in 2D cylindrical coordinates (modified from Holliger and Bergmann, 2002). The electric- and magnetic-field components are located at the edges and the centre of a cell such as that denoted by dotted lines.

and right-hand sides of the simulation grid (Berenger, 1994; Sullivan, 2000). We base our analyses on the same canonical models as used in Holliger and Bergmann (2002): a homogeneous medium ($\varepsilon = 9\varepsilon_0$, $\sigma = 1$ mS m^{-1}) containing air-filled borehole ($\varepsilon = \varepsilon_0$, $\sigma = 0$ S m^{-1}) or water-filled borehole ($\varepsilon = 80\varepsilon_0$, $\sigma = 1$ mS m^{-1}).

With the assumed cylindrical symmetry, the transmitter antenna and its borehole, which are centred on the z-axis, can be explicitly and accurately represented with the above approach. In this paper, a dipole antenna is used as the transmitter antenna. It consists of two metal arms. A dipole antenna functions by having current run through the arms, which results in radiation. FDTD simulates a dipole antenna in the following way: The metal of the arms is specified by setting its E_z field to be zero, which ensures that conductivity is infinite in the corresponding metal cells. The source is specified by setting the E_z field in the gap, the cell between the two arms, to a certain value. For simplicity, we specify a Gaussian voltage pulse $V(t)$ as (Sullivan, 2000; Ellefsen and Wright, 2005)

$$V(t) = \exp\left[-\frac{(t - t_0)^2}{2\tau^2}\right] \tag{12}$$

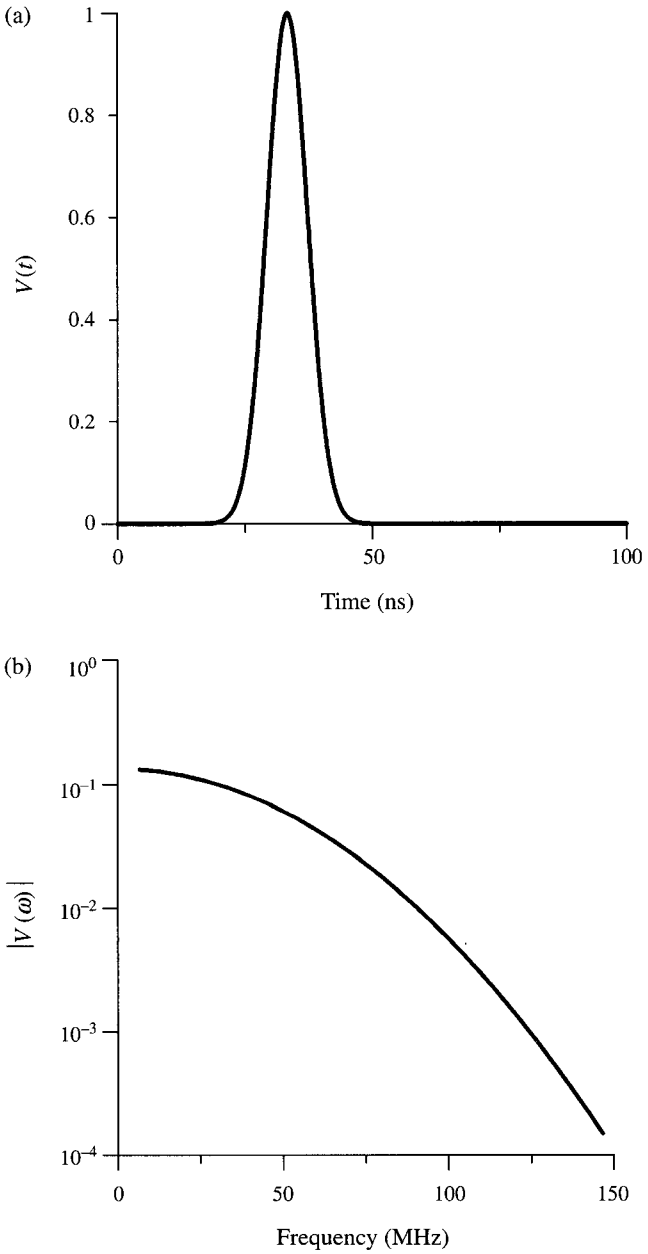

Fig. 2. (a) Voltage used for FDTD simulations, and (b) power spectrum of the voltage. The spectrum is normalised by its maximum value.

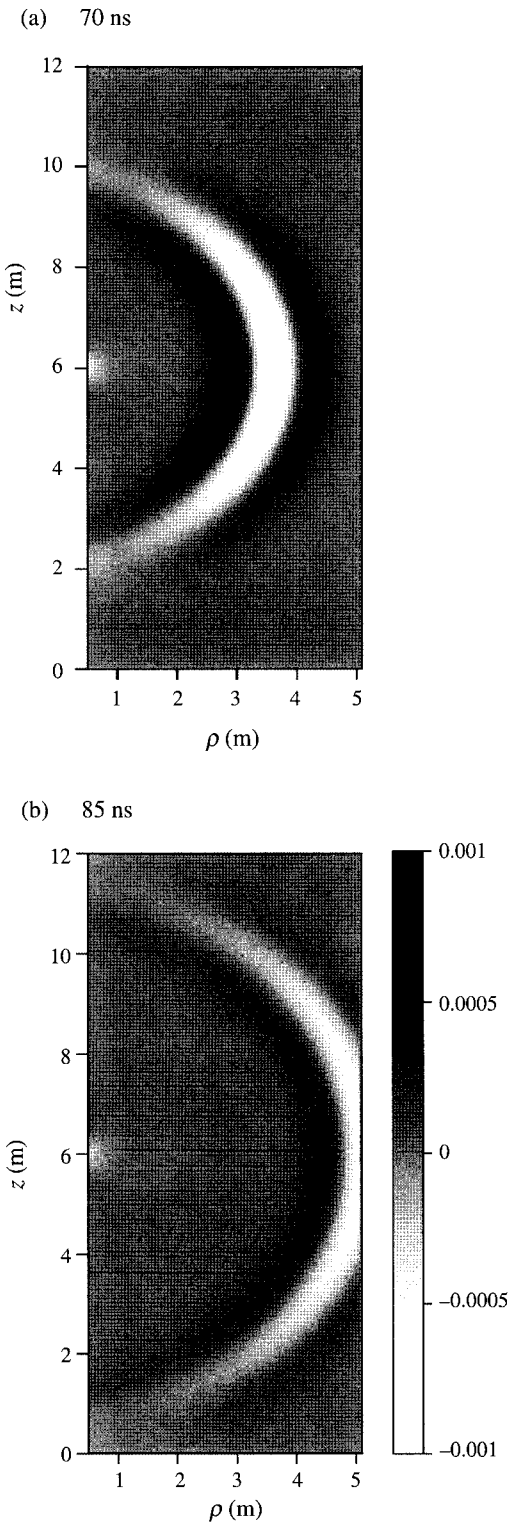

Fig. 3. Snapshots of E_z fields at (a) 70 ns and (b) 85 ns for a homogeneous model. Outgoing waves, generated from a 20 cm dipole antenna at $z = 6$ m in an air-filled borehole having a diameter of 9 cm, remain concentric. Only when the wave gets within eight points of the top, bottom, and right-hand edges, which are inside PML, does distortion start to occur.

where τ is a pulse width, and t_0 is an appropriate time shift to ensure causality, to define the source field

$$E_z(t) = -V(t)/\Delta z \tag{13}$$

at the gap. In this paper, we assign $t_0 = 33.3$ ns and $\tau = 4$ ns, except for the last case, which examines effect of pulse width on waveguide behaviour. With these values, the source voltages are significant between 18 ns and 51 ns (Figure 2a). In the frequency domain, the amplitude decreases gradually as the frequency increases (Figure 2b).

The received signal was represented by the electric field at the observation point. Figure 3 shows snapshots of E_z fields initiated from a 20 cm dipole antenna in an air-filled borehole with a diameter of 9 cm. As the wave reaches the PML, which is eight cells thick on top, bottom, and right-hand sides, it is absorbed. The effectiveness of the PML is apparent in the right figure, because the image would not be concentric circles if the outgoing wave partially reflected.

As Holliger and Bergmann (2002) pointed out, resonance effects due to a dry borehole should not be significant provided that the EM-wave velocity in the borehole is faster than in the embedding medium. The situation is, however, completely different in the presence of a water-filled borehole. The dielectric constant of water is much higher than that of the surrounding material and thus water in a borehole functions as a waveguide for EM waves. The mechanism of the waveguide is similar to the 'tube wave' in borehole seismic. The guided wave is a wave for a cylindrical interface between the two media. In this regard, the numerical scheme developed here is suitable for modelling waveguide effects.

Figure 4 shows transmitted pulses and their amplitude spectra. The EM wavefields are generated from a 20 cm dipole antenna located in the centre of source borehole with a diameter of 9 cm and observed at a point of 5 m horizontally away from the source antenna. In the illustrations, the EM waveforms and the spectra are normalised by the maximum amplitude of first-cycle direct wave and by that of source signal shown in Figure 2, respectively.

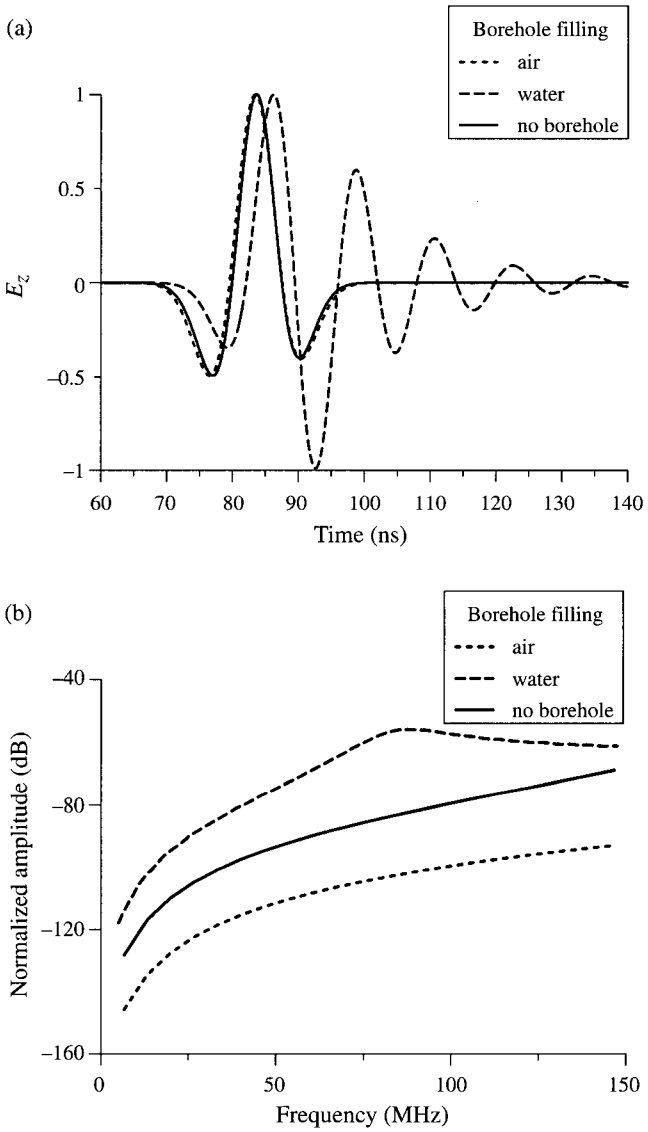

Fig. 4. Normalised vertical electric fields (a) and their power spectra (b) at a point of 5 m from the centre of a 20 cm transmitter antenna located in air- and water-filled boreholes with a diameter of 9 cm.

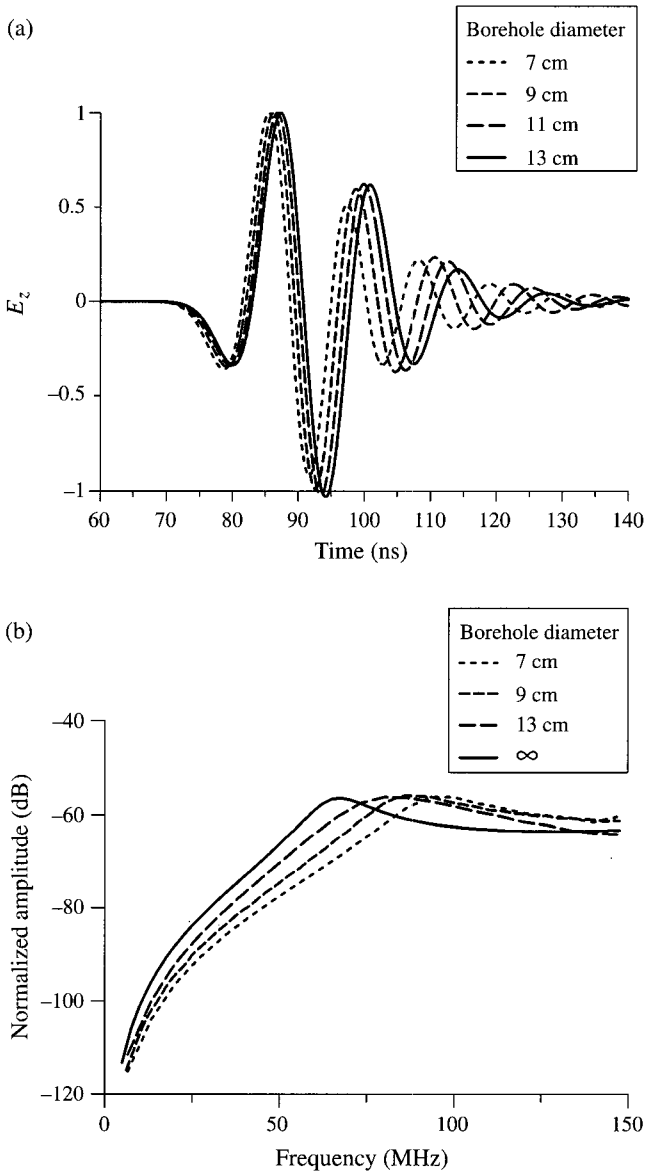

Fig. 5. Normalised vertical electric fields (a) and their power spectra (b) at a point of 5 m from the centre of a 20 cm transmitter antenna located in a water-filled borehole with diameters of 7, 9, 11, and 13 cm.

A reverberatory character can be found after the first cycle of the pulse only in the case of water-filled borehole. This is because the water-filled borehole acts as a waveguide. The amplitude of the reverberation becomes smaller with time. An air-filled borehole produces no clear reverberation, and the waveform has the shape of a Ricker wavelet. This is the same outcome as in the case of a homogeneous reference model without borehole. Furthermore, the shapes of radiated waves are essentially indistinguishable between the air-filled borehole and homogeneous full-space cases. The spectrum shapes for these two models are also similar to each other, but the water-filled borehole produces a spectrum peak at about 85 MHz.

Behaviour due to a borehole waveguide is often observed in borehole radar measurements. The phenomenon deforms the antenna pattern and can cause artefacts in radar measurements (Ebihara et al., 1998). A water-filled borehole can function as a waveguide for EM waves under some conditions. The waveguide effects depend strongly on the length of the transmitter antenna, the medium filling the borehole, and the diameter of the borehole.

Figure 5 compares normalised E_z fields measured at 5 m from boreholes with various diameters: 7, 9, 11, and 13 cm. A clear reverberatory character can be seen after the direct wave (Figure 5a). The reverberations gradually decay with time. Furthermore, the pulse length of the reverberations becomes longer with increasing borehole diameter. The effect of the borehole on the reverberations is also recognisable in the frequency domain (Figure 5b). The water-filled borehole produces peak amplitudes at about 80 MHz in the spectrum, and the peak shifts to lower frequencies, approaching the resonance frequency of 67 MHz in water, as the borehole diameter increases. These findings imply that borehole measurements may be optimised by choosing the observation frequency, taking into account the borehole diameter if the borehole is filled with water.

Figure 6 compares the normalised maximum first-cycle amplitudes of synthetic wavefields along a vertical line at a distance of 5 m from the symmetry-axis for the models containing water-filled boreholes with the amplitudes for a model having an air-filled borehole. The radius of the air-filled borehole has little effect on the normalised amplitude compared with the radius effect for the reference model. In contrast, water-filled boreholes can distort the radiation amplitude, and the resulting amplitudes increase with the radius of the water-filled borehole.

Antennas of different lengths are simulated in order to examine the effect of antenna length in water-filled boreholes on the waveguide effect. Figure 7 compares transmitted pulses and their spectra generated from 10 cm, 20 cm, and 30 cm long antennas located in a water-filled borehole with a diameter of 9 cm, and Figure 8 shows radargrams collected along a vertical line at a distance of 5 m from the symmetry-axis of the borehole. The longer the transmitter antenna, the more pronounced the reverberatory character (Figure 7a), and the lower the peak amplitude frequency (Figure 7b). Note that the 10 cm long antenna generates little reverberation, and thus shows no clear peak in the spectrum.

Figure 9 illustrates the effect of the pulse width of the source signal on radiated wavefields. Three pulse widths of $\tau = 4$, 5, and 6 (ns) are considered, and their resulting radiated waves are collected at a point of 5 m from the centre of a 20 cm antenna located in a water-filled borehole with a diameter of 9 cm. The source pulse width strongly affects the amplitude variations of the resulting guided waves. The amplitudes of reverberated waves decay more rapidly as the pulse width increases. In the frequency domain, however, the normalised amplitude

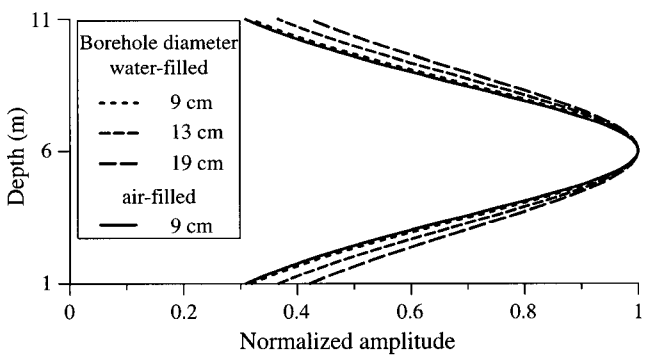

Fig. 6. Normalised maximum first-cycle amplitudes observed along a vertical line at a distance of 5 m from the centre of a 20 cm transmitter antenna located in air- (solid) and water-filled (dashed) boreholes. The diameters of air- and water-filled boreholes are set to 9, 13, and 19 cm, respectively.

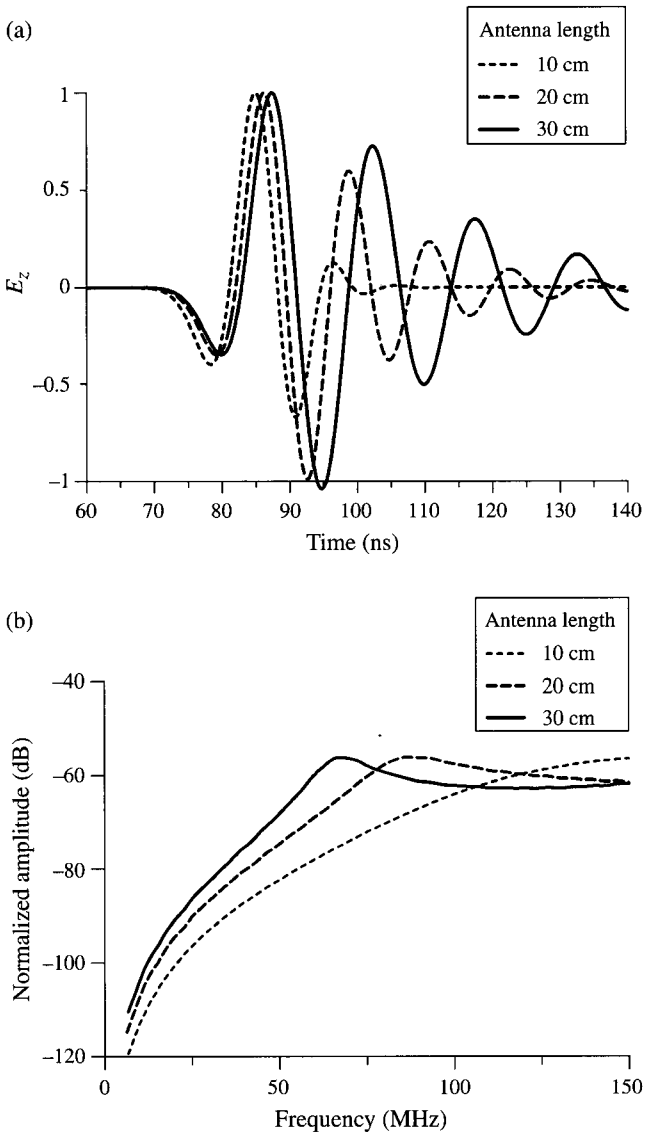

Fig. 7. Normalised vertical electric fields (a) and their amplitude spectra (b) at a point of 5 m from the centre of a water-filled borehole with a diameter of 9 cm. The transmitted pulses are generated from dipole antennas of 10 cm, 20 cm, and 30 cm long in the borehole.

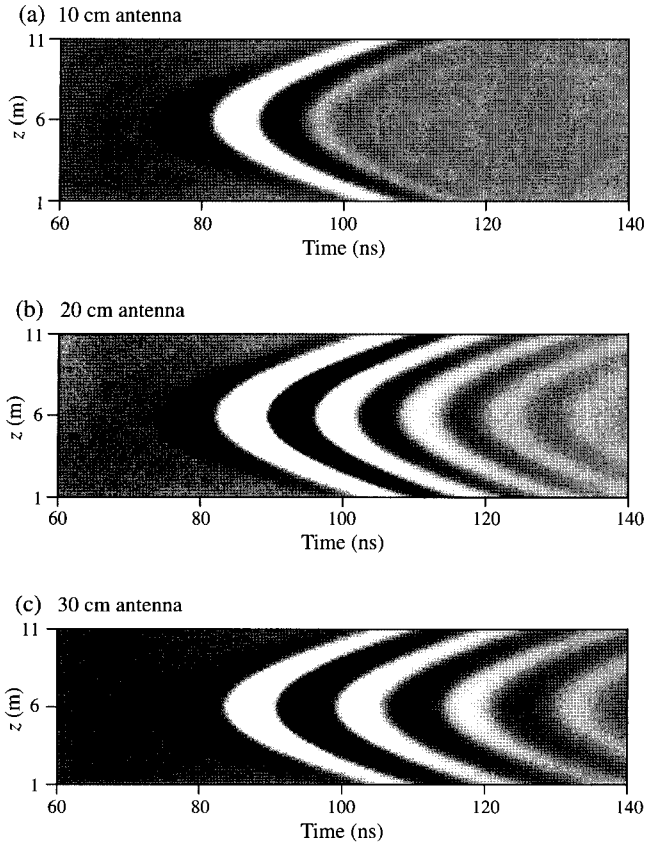

Fig. 8. Radargrams consisting of the E_z-component of the EM wavefield radiated from a transmitter antenna located in a water-filled borehole with a diameter of 9 cm. Three antenna lengths are considered: (a) 10 cm, (b) 20 cm, and (c) 30 cm. The data are collected along a vertical line at a distance of 5 from the symmetry-axis.

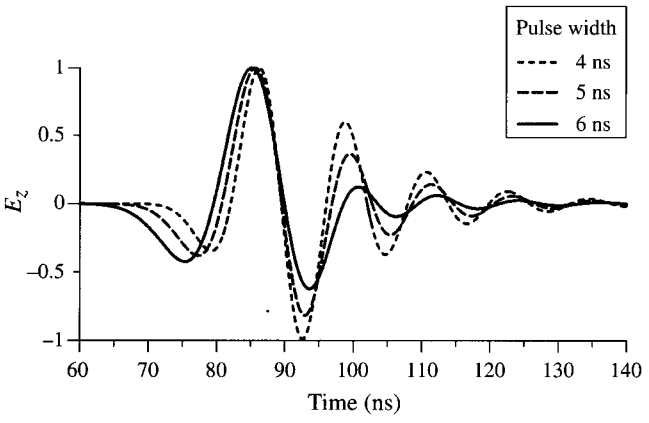

Fig. 9. Normalised vertical electric fields at a point of 5 m from the centre of a 20 cm transmitter antenna located in a water-filled borehole with a diameter of 9 cm. Three pulse widths are considered: $\tau = 4$, 5, and 6 ns.

spectrum is independent of the pulse width, as is shown in Figures 5b or 7b.

Conclusions

We have presented a FD solution of Maxwell's equations in cylindrical coordinates which is suitable for modelling crosshole GPR data. This algorithm was used to model the EM wavefield radiated from a vertical electric antenna located in a borehole filled with air or water. Major simplifications made in this study were that only the radiation pattern of the transmitter was accounted for explicitly and that the received signal was represented by the electric field at the observation point. The radiation pattern of an antenna located in a water-filled borehole is severely distorted by a waveguide effect that depends on the length of the transmitter antenna, the medium filling the borehole, and the diameter of the borehole. Given that most shallow boreholes are at least partially water-filled, this has potentially serious implications for the interpretation of crosshole GPR data. Further complications of the radiation pattern, regardless of the medium filling the borehole, must be expected to arise from vertical stratification and lateral heterogeneity of electric parameters in the shallow subsurface.

Acknowledgments

This work was supported by the KOSEF-JSPS Cooperative Program (F01–2006–000–10248–0). We thank Dr Takao Kobayashi, Dr Jung-Ho Kim, and an anonymous reviewer for helpful comments and suggestions.

References

Alumbaugh, D., and Chang, P. Y., 2002, Estimating moisture contents in the vadose zone using cross-borehole ground penetrating radar: A study of accuracy and repeatability: *Water Resources Research* **38**, 1309. doi: 10.1029/2001WR000754

Berenger, J. P., 1994, A perfectly matched layer for the absorption of electromagnetic waves: *Journal of Computational Physics* **114**, 185–200. doi: 10.1006/jcph.1994.1159

Bergmann, T., Blanch, J. O., Robertsson, A., and Holliger, K., 1999, A simplified Lax-Wendroff correction for staggered-grid FDTD modeling of electromagnetic wave propagation in frequency-dependent media: *Geophysics* **64**, 1369–1377. doi: 10.1190/1.1444642

Day-Lewis, F. D., Lane, J. W., Harris, J. M., and Gorelick, S. M., 2003, Time-lapse imaging of saline tracer transport in fractured rock using difference radar attenuation tomography: *Water Resources Research* **39**, 1290. doi: 10.1029/2002WR001722

Ebihara, S., Sato, M., and Niitsuma, H., 1998, Analysis of a guided wave along a conducting structure in a borehole: *Geophysical Prospecting* **46**, 489–505. doi: 10.1046/j.1365-2478.1998.00104.x

Ellefsen, K. J., and Wright, D. L., 2005, Radiation pattern of a borehole radar antenna: *Geophysics* **70**, K1–K11. doi: 10.1190/1.1852779

Ernst, J. R., Holliger, K., Maurer, H., and Green, A. G., 2006, Realistic FDTD modelling of borehole georadar antenna radiation: methodology and application: *Near Surface Geophysics* **4**, 19–30.

Fullagar, P. K., Livelybrooks, D. W., Zhang, P., Calvert, A. J., 2000, Radio tomography and borehole radar delineation of the McConnell nickel sulfide deposit, Sudbury, Ontario, Canada: *Geophysics* **65**, 1920–1930. doi: 10.1190/1.1444876

Holliger, K., and Bergmann, T., 2002, Numerical modeling of borehole georadar data: *Geophysics* **67**, 1249–1257. doi: 10.1190/1.1500387

King, R. W. P., and Smith, G. S., 1981, *Antennas in Matter: Fundamentals, Theory, and Applications*, MIT Press.

Moran, M. L., and Greenfield, R. J., 1993, Radar signature of a 2.5-D tunnel: *Geophysics* **58**, 1573–1587. doi: 10.1190/1.1443373

Moysey, S., and Knight, R. J., 2004, Modeling the field-scale relationship between dielectric constant and water content in heterogeneous systems: *Water Resources Research* **40**, W03510. doi: 10.1029/2003WR002589

Olhoeft, G. R., 1988, Interpretation of hole-to-hole radar measurements: *Proceedings of the 3rd Symposium on Tunnel Detection*, pp. 616–629.

Olsson, O., Falk, L., Forslund, O., Lundmark, L., and Sandberg, E., 1992, Borehole radar applied to the characterization of hydraulically conductive fracture zones in crystalline rock: *Geophysical Prospecting* **40**, 109–116. doi: 10.1111/j.1365-2478.1992.tb00367.x

Pratt, R. G., and Worthington, M. H., 1988, The application of diffraction tomography to cross-hole seismic data: *Geophysics* **53**, 1284–1294. doi: 10.1190/1.1442406

Sato, M., and Thierbach, R., 1991, Analysis of a borehole radar in cross-hole mode: *IEEE Transactions on Geoscience and Remote Sensing* **29**, 899–904. doi: 10.1109/36.101368

Sullivan, D.M., 2000, *Electromagnetic Simulation Using the FDTD Method*, IEEE Press.

Tronicke, J., Holliger, K., Barrash, W., and Knoll, M.D., 2004, Multivariate analysis of cross-hole georadar velocity and attenuation tomograms for aquifer zonation: *Water Resources Research* **40**, W01519. doi: 10.1029/2003WR002031

Williamson, P.R., and Worthington, M.H., 1993, Resolution limits in ray tomography due to wave behaviour: *Geophysics* **58**, 727–735. doi: 10.1190/1.1443457

Yee, K.S., 1966, Numerical solution of initial boundary value problems involving Maxwell's equations in isotropic media: *IEEE Transactions on Antennas and Propagation* **14**, 302–307. doi: 10.1109/TAP.1966.1138693

Zhou, C., Cai, W., Luo, Y., Schuster, G., and Hassanzadeh, S., 1995, Acoustic wave-equation traveltime and waveform inversion of crosshole seismic data: *Geophysics* **60**, 765–773. doi: 10.1190/1.1443815

Manuscript received 8 December 2006; accepted 19 January 2007.

Appendix

Ampere's law describes the relationship between magnetic field components along a closed elemental contour C, bounding the corresponding open element surface S, with the electric field distribution on that surface (Figure A1), and

$$\begin{aligned}\oint_C \mathbf{H}\cdot \mathrm{d}S &= \int_S \left(\varepsilon\frac{\partial \mathbf{E}}{\partial t}+\sigma\mathbf{E}\right)\cdot \mathbf{n}\,\mathrm{d}S\\ &= \left(\varepsilon_1\frac{\partial E_z}{\partial t}+\sigma_1 E_z\right)\Delta x l_1+\left(\varepsilon_2\frac{\partial E_z}{\partial t}+\sigma_2 E_2\right)\Delta x l_2,\\ &= \left(\bar{\varepsilon}\frac{\partial E_z}{\partial t}+\bar{\sigma}E_z\right)\Delta x\Delta y\end{aligned}$$

where

$$\bar{\varepsilon}=\frac{\varepsilon_1 l_1+\varepsilon_2 l_2}{\Delta y},\qquad \bar{\sigma}=\frac{\sigma_1 l_1+\sigma_2 l_2}{\Delta y}$$

In particular, when $l_1=l_2=\Delta y/2$,

$$\bar{\varepsilon}=\frac{\varepsilon_1+\varepsilon_2}{2},\qquad \bar{\sigma}=\frac{\sigma_1+\sigma_2}{2}$$

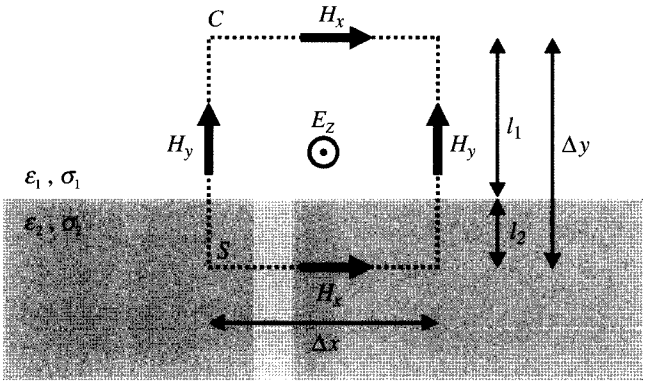

Fig. A1. Schematic representation of the Ampere's Law integral expression near the interface between two different media.

시추공간 레이다 측정에서 전자기 도파관 효과의 수치모델링

장한누리, 박미경, 김희준

요 약: 시추공 지중레이다 고주파수 전자기파 전파와 관련된 현상은 복잡하다. 그 물리적 과정을 보다 잘 이해하기 위해서 본 연구에서는 원통좌표계에서 맥스웰방정식의 유한차분 시간영역 해를 이용하였다. 이 방법은 시추공간 레이다탐사에서 전자기파의 전파형을 모델링할 수 있다. 그리고 원통좌표계는 계산 효율이 높고, 파동장의 3 차원적인 기하학적 확산을 정확하게 계산할 수 있으며, 또 작은 크기의 시추공을 이산화할 때 효과적이다. 수치계산 결과를 통해 물로 채워진 시추공은 전파 파형에 영향을 주는 강한 도파관 효과를 일으킬 수 있으며, 그 도파관 효과는 시추공의 크기와 안테나의 길이 에 의존한다.

주요어 : 시추공간, 지중 레이다, 유한차분 시간영역, 원통좌표계

クロスホールレーダ測定における電磁導波管効果の数値モデリング

張 ハンヌリ（チャン・ハンヌリ）・朴 美京（パク・ミキョン）・金 喜俊（キム・ヒジュン）

要 旨: ボアホールレーダにおける高周波数電磁波の伝播に関する現象は複雑である。その物理過程をより理解する為に，本研究では円筒座標系におけるマクスウェル方程式の有限差分，時間領域解を利用した。この方法は，クロスホールレーダ探査における電磁波の全波形をモデリングすることが出来る。円筒座標系は計算効率が高く，波動場の 3 次元的な幾何学的拡散を正確に計算することが出来，また小さなボアホールを離散化するのに効果的である。数値計算の結果，水で満たされたボアホールは伝播波形に影響を与える強い導波管効果を引き起し，その導波管効果はボアホールの大きさ，アンテナの長さに依存する。

キーワード：坑井間，レーダ，有限差分，時間領域，円筒座標系

부경대학교, 환경탐사공학과
608-737 부산시 남구 대연동 559-1,

釜慶大学校環境海洋大学　地球環境科学群環境探査工学科